# Weakly Dispersive Hydraulic Flows in a Contraction - Parametric Solutions and Linear Stability

Bernard K. Ee and Simon R. Clarke

*School of Mathematical Sciences, Monash University, Clayton, Victoria 3168, Australia.*

## Abstract

We consider the propagation of stratified fluid through a contraction near resonance, for which the governing asymptotic equation is the forced KdV equation. Steady solutions of this equation are sought which have constant, but differing amplitudes upstream and downstream of the contraction, and for which leading order dispersive effects are retained. A numerical algorithm is outlined to obtain such solutions, yielding a parametric relationship between the normalized velocity perturbation and the normalized width perturbation. Matrix methods are then used to investigate the linear stability of these solutions.

## I. INTRODUCTION

The study of stratified fluid flows through a contraction is of significance in both oceanographic and engineering contexts, such as the study of deep overflows in the ocean, flows in estuaries and flow within and between reservoirs to name a few. Baines[1] details the general theory of stratified flow over topography as well as applications and the interested reader is urged to consult that monograph. The physical context of this paper is to consider the propagation of stratified fluid through a contraction at a speed near a long wave speed, i.e. flow is near resonance. What typically results is a transition of flow characteristics within the contraction yielding hydraulic flows, characterised by different upstream and downstream mean levels. However in reality, dispersive waves will occur resulting in standing waves being superimposed on these solutions due to the finite length of the contraction.

As considered here, a hydraulic solution is generally one where the fluid response is a function of some perturbation variable, e.g. depth or contraction width. While it is possible to have symmetric hydraulic solutions, the solutions of interest here are those which are topographically controlled[2]. Such solutions are characterized by a zero long wave speed at the perturbation maximum and consequently match smoothly with the upstream subcritical and downstream supercritical solutions. Dispersive hydraulic solutions, as of interest here, are those where the same occurs but leading order dispersive effects are retained. In this case, standing waves are possible but the solutions of interest are those which have no waves superimposed, and so, the fluid response is effectively only a function of the topographic perturbation, as for hydraulic solutions. In fact, the purpose of this paper is to study these solutions in the weakly nonlinear limit and the effect of the contraction on the formation of these solutions.

A general derivation for the long wave limit of weakly nonlinear stratified flow through a contraction is presented in Clarke and Grimshaw[3]. It was demonstrated there that flow through horizontal contractions, where either the oncoming velocity or contraction width were a function of height, was equivalent to flow over vertical contractions. For such flows, the amplitude of the resonant internal wave mode is governed by the forced Korteweg-de Vries (fKdV) equation:

$$B_\tau + \Delta B_x + 6BB_x + B_{xxx} = -\gamma f_x, \tag{1}$$

where $x$, $\tau$ are the spatial and time variables respectively, $\Delta$ is a detuning parameter quantifying the difference between the flow velocity and the long wave speed and $\gamma$ is the coefficient of the forcing term, $f$. Consider as an example, two-layer flow past a topographic perturbation in the Boussinesq limit. We assume that the dimensionless undisturbed lower layer depth is $R$ and the height of the topography is $R\epsilon f(\mu x)$. Then following Baines[1], the scaled interface displacement will satisfy (1) where

$$\Delta = -\frac{6}{\mu^2 d_s}(Fr-1), \quad \gamma = \frac{9\epsilon^{1/2}}{2d_s^2\mu^2(1-2R)}, \quad d_s = R(1-R).$$

and the Froude number, $Fr$, is based on the linear long wave speed.

Here we will concentrate on symmetric bell-shaped forcing functions $f(x-x_p)$, where $x_p$ is the peak of the forcing and $x > x_p$ and $x < x_p$ denote the upstream and downstream regions respectively while $f$ satisfies $0 \leq f \leq 1$, $f \to 0$ as $|x| \to \infty$ and $f(0) = 1$. For such forcings, Grimshaw and Smyth[4] (henceforth referred to as GS) considered in detail the solutions of (1) for the zero initial condition, which we now briefly describe. The boundaries of the solution regions are such that when $|\gamma| \to 0$, $\Delta$ is proportional to $|\gamma|^{2/3}$, while as $|\gamma| \to \infty$, $\Delta$ is proportional to $|\gamma|^{1/2}$. This dependence was explicitly demonstrated for $\gamma > 0$ where asymptotic solutions were constructed. These solutions consisted of steady dispersive hydraulic solutions in the vicinity of the topography, matched upstream and downstream to modulated wavetrains.

The assumption in GS appears to be that dispersive hydraulic solutions exist for intermediate positive $\gamma$ values, although the existence of a continuum of such solutions has not been established. The question of the existence of dispersive hydraulic solutions for negative $\gamma$ values and their corresponding linear stability in general have not been previously considered.

There are several relevant recent papers which discuss the fKdV equation and in particular the steady hydraulic type solutions of (1). Numerous references to the fKdV equation in general can be found in Baines[1] and in the following papers. First, Dias and Vanden-Broeck[5] considered critical free surface flows in scenarios where there were supercritical upstream and wavy solutions downstream. The hydraulic flow solution is the limiting case, i.e. when downstream waves disappear. In their subsequent work, Dias and Vanden-Broeck[6,7] considered the dynamics of interfacial waves, in which two contiguous homogeneous fluids, of different densities and layer thickness, flow over an obstacle. Further, Dias and Vanden-Broeck[8]

considered the flow past two obstacles of arbitrary shape and showed that the resulting solution was characterised by supercritical flow on one side of the obstacle and a train of waves trapped between these two obstacles. These solutions were described as generalized hydraulic falls in the latter paper and were shown to hold when the distance between the two obstacles is large. In general, these works by Dias and Vanden-Broeck seek solutions with waves downstream which then re-connect to form these hydraulic solutions. As will become apparent, this is similar to the periodicity condition imposed in this paper.

The stability of solitary wave solutions of the fKdV equation with compact support was first considered by Bona et al[9], who used the Hamiltonian of the fKdV equation along with the conserved quantities of mass and momentum to determine the stability of the solitary wave solution. Pego and Weinstein[10] studied the linear eigenvalue problem for the stability and related it to the derivative of the momentum of the solitary wave. Camassa and Wu[11] considered the stability of steady and forced solitary waves. Their approach involved first finding the parameters in the evolution equation for the perturbation term for which we have zero eigenvalues and then applying branch following methods to determine the full eigenvalue spectrum. The method of Pego and Weinstein[10] was subsequently generalized by Pelinovsky and Grimshaw[12] to an integro-differential generalization of the KdV equation.

Hence, the objective of this paper is two-fold. First, we search for steady weakly dispersive analogues of hydraulic flows that solve (1), subject to a forcing $f$. In so doing, we aim to obtain a $\Delta(\gamma)$ parametric curve which describes the steady dispersive hydraulic solutions in $-\gamma_1 \leq \gamma \leq \gamma_2$ where $\gamma_1,\ \gamma_2 >> 1$ and verify the two analytical limits of $\gamma \to 0$ and $\gamma \to \infty$ obtained by GS. To this end in Sec. II, some relevant properties of the fKdV equation are discussed. Details of the branch following algorithm used to obtain the dispersive hydraulic solutions are provided in Sec. III and the continuum of the solutions is discussed in Sec. IV. The second objective is to investigate the linear stability of these solutions. Thus we are effectively considering the solutions of the fKdV equation with small perturbations to dispersive hydraulic solutions as the initial condition. This is in contrast to GS who considered solutions of the fKdV equation for a zero initial condition. In Sec. V, the stability of dispersive hydraulic solutions is considered using matrix methods. We note that previous methods to study the stability of the fKdV equation and its generalizations are not necessarily applicable here, due to the solutions not having compact support of forced solitary waves. The implications of these results are discussed in the conclusion.

## II. PROPERTIES OF THE FORCED KDV

Consider the general forced KdV equation

$$A_\tau + UA_x + rAA_x + sA_{xxx} = -G_0 f_x(\xi(x - x_p)). \tag{2}$$

where $f$ is a bell-shaped forcing of magnitude unity, as described earlier, $G_0$ is the coefficient of the forcing and $\xi$ is a characteristic inverse lengthscale of the forcing. This was the definition of the forcing used in GS. This can be reduced to a two-parameter system by introducing $\tilde{x} = \xi x$, $A(x, \tau) = \delta B(x, \tau) + A_0$ and $\tilde{\tau} = \xi\delta r/6$ where $(r\delta)/(s\xi^2) = 6$ and $A_0$ is some characteristic upstream amplitude. Then, $B$ satisfies (1) where

$$\Delta = \frac{6(U + rA_0)}{r\delta}, \quad \gamma = \frac{6G_0}{r\delta^2}.$$

and the tildes are dropped for the scaled independent variables $x$ and $\tau$. Here, $\Delta$ and $\gamma$ represent respectively appropriately scaled detuning and forcing parameters. The limits $\xi \to 0$ (hydraulic) and $\xi \to \infty$ (narrow topography), considered by GS, correspond respectively to $\gamma \to \infty$ (large topography) and $\gamma \to 0$ (small topography). The initial condition to be considered later is that of a steady dispersive hydraulic solution.

For a particular initial condition, be it a steady dispersive hydraulic solution or the trivial initial condition, the various types of flows which can occur must be a function of the scaled parameters $\Delta$ and $\gamma$. So the flow regimes for steady and unsteady flows must be given by a parametric relationship $F(\gamma, \Delta) = 0$. GS and subsequent papers have classified much of the unsteady behaviour for (1). As stated in Sec. I, the first goal of this paper is to obtain a parametric relationship for steady dispersive hydraulic solutions. Hence, we ignore the time derivative term and integrating (1) with respect to $x$ then gives

$$\Delta B + 3B^2 + B_{xx} = -\gamma f, \tag{3}$$

where it has been assumed without loss of generality that the far upstream amplitude is $B = 0$. Ignoring topographic effects in the far-field, we have

$$\Delta B + 3B^2 + B_{xx} = 0, \tag{4}$$

which has two critical points $B = 0$ and $B = -\Delta/3$. For $\Delta > 0$, these correspond respectively to a centre and a saddle point. This is reversed for $\Delta < 0$. Since we can transform the latter case to the former through the addition of a mean level, we can therefore assume that $\Delta \geq 0$ for hydraulic solutions and hence the steady flow solutions that are sought are subcritical upstream and supercritical downstream, leading to asymmetric and dispersive hydraulic solutions of the fKdV equation.

Assuming that we have such solutions for symmetric topography, the symmetries show that the reflected version of this solution also satisfies the fKdV equation. Hence if a second topographic perturbation is placed far downstream then it is possible to construct a periodic solution consisting of the original solution at the upstream topography and a reflected solution at the downstream topography. A sample of this periodic solution is given in Figure 1. For these periodic solutions, we denote the original solution region as $0.5x_u \leq x \leq x_u$ and the reflected region as $0 \leq x \leq 0.5x_u$. In general, it is assumed that the topographic perturbations are centered at $x = 0.75x_u$ and $x = 0.25x_u$. In the original region, due to the assumption of $\Delta \geq 0$, an asymmetric dispersive hydraulic solution will have a mean increase in amplitude as a function of $x$ over the topographic perturbation. Such solutions are referred to as upward jumps and the corresponding solution in the reflected region, a downward jump.

One concern about the construction of such a periodic solution is the possible interaction of the tails of the original and reflected solutions at $x = x_u/2$. We shall show in Sec. III that this interaction is typically very small. The periodicity of the combined solution allows us to avoid the generally asymmetric nature of steady, dispersive hydraulic solutions and to apply Fourier spectral methods. Hence, standard matrix methods can then be used to determine the linear stability of the combined periodic solution. These will be described in greater detail in Sec. V.

Before considering the continuum of dispersive hydraulic solutions, we outline the approximate solutions of the steady fKdV equation of GS for our forcing. The narrow forcing limit of GS corresponds to small values of $\gamma$. In this limit, we can integrate over the forcing and match the steady solutions of the KdV equation over this singularity. If $K = \int_{-\infty}^{\infty} f dx$, then steady solutions exist for $\Delta$ and $\gamma$ given by

$$(\frac{\Delta}{3})^3 = (K\gamma)^2. \tag{5}$$

This approximation is valid for the limits $\gamma \to 0^{\pm}$, although GS only considered $\gamma \to 0^{+}$. The wide forcing limit corresponds to large and positive $\gamma$ values. Here, we ignore the dispersive term in (3) and are thereby considering hydraulic solutions. In this case, $B$ satisfies a quadratic equation which can be matched at the topographic maximum. In our notation, solutions only occur when

$$\Delta = \sqrt{12\gamma}. \tag{6}$$

For the $\mathrm{sech}^2(x)$ forcing we shall use, a solitary wave solution of the form $D = a\mathrm{sech}^2(x - x_p)$ where $a$ is some constant coefficient also exists, see Camassa and Wu[11]. Setting $\Delta = 0$, (3) reduces to

$$(3a^2 - 6a)\mathrm{sech}^4(x - x_p) + (4a + \gamma)\mathrm{sech}^2(x - x_p) = 0 \tag{7}$$

Then either $\gamma = -4a$ and $a = 0, 2$, which in turn implies that $\gamma = 0, -8$. Therefore the only non-trivial solution of this form is for $\gamma = -8$.

Finally, we should note that we were able to numerically determine one further symmetric solution in which $\Delta = 0$ and this was found to occur at $\gamma \approx -24.55$. This will be discussed later.

## III. NUMERICAL PROCEDURE AND PARAMETRIC RELATIONSHIP

Here we outline the numerical procedure for solving (3) such that the solutions are generally asymmetric, dispersive hydraulic flows. The numerical procedure is characterized by four levels, namely ODE integration, minimization algorithm, solution refinement and a branch following algorithm. Let $B_u$ denote the far-field upstream amplitude and $B_d$ denote the far-field downstream amplitude. The problem at hand is to find hydraulic type solutions such that $B_u = 0,\ B_d = -\Delta/3$ and the gradient of the amplitude in the far-field is $B_{ux},\ B_{dx} = 0$ respectively. We assume for given $\gamma$ this only occurs for particular $\Delta$, which then leads to a parametric curve $\Delta(\gamma)$. It should be noted that (3) is a three-dimensional dynamical system and what we are seeking is a unique trajectory for that system starting at the centre for large $x$ and finishing at a saddle point for $x$ large and negative. We cannot start the integration from a saddle point because, as will be shown later, this does not capture the downstream influence which occurs for these solutions. Hence, the difficulty of

this problem is shooting to the unstable downstream point. This causes standard methods such as the Newton-Raphson to fail.

### A. ODE Integration

The integration of (3) employs a shooting method implemented from the upstream region to the downstream region. The Runge-Kutta (4,5) method was used, based on the Dormand-Prince pair[13], as implemented in MATLAB. We can assume, in general, that there is no upstream influence on the upstream side of the topography, so dispersion is negligible when the topography is negligible. Hence, the upstream starting point simply needs to be sufficiently upstream so that the topographic perturbation is negligible. On the downstream side of the topography, waves occur outside the region where the topography is significant. However, we still only need to shoot to sufficiently downstream such that the topographic effect is negligible. The output of this routine is the downstream amplitude, $B_d$ and $B_{dx}$, as functions of the input parameters $\gamma$ and $\Delta$.

### B. Minimization algorithm

Consider the nature of the downstream point. Let us define the Hamiltonian of (3) as

$$V(B, B_x) = \gamma f B + \frac{1}{2}B_x^2 + \frac{1}{2}\Delta B^2 + B^3. \tag{8}$$

In the far-field, $V_c = V(-\Delta/3, 0) = \Delta^3/54$ downstream and $V_c = 0$ upstream. Referring to Figure 2, we want to find a minimum $\Delta$ so that the far-field downstream amplitude lies within the hatched region and ideally on the homoclinic orbit. If this occurs, then we have effectively reached the saddle point. Note the size of the homoclinic orbit increases with $\Delta$ since we have assumed that $\Delta > 0$. To ensure that the downstream amplitude solution lies within the homoclinic orbit, we can specify two conditions:

$$V(V - V_c) \leq 0 \tag{9a}$$

$$|B| \leq |\Delta/3| \tag{9b}$$

The justification for (9) is evident from consideration of Figure 2 for two reasons. First, for the solution to be contained in the homoclinic orbit, $V$ must lie between the local maximum

$V_c$ and the local minimum $V = 0$. Secondly, within the homoclinic orbit $-\Delta/3 \leq B \leq \Delta/6$, which is satisfied if (9a) or (9b) are both satisfied.

Since the conditions (9) are highly nonlinear functions of the input parameters $\Delta$ and $\gamma$, it has been found that the following algorithm based on bracketing and bisection is the most efficient method to obtain a solution for given $\gamma$:

(i) Let $\Delta_1$ be such that either one of (9) is not satisfied and $\Delta_2 > \Delta_1$ that satisfies (9).

(ii) Divide $[\Delta_1,\ \Delta_2]$ into $n$ intervals.

(iii) Apply the shooting algorithm, starting with $\Delta_2$ and moving in the direction of decreasing $\Delta$ along the interval in (ii) until we have a value of $\Delta$ such that either one of the conditions in (9) is not satisfied. Let us denote the $\Delta$ value at which this occurs to be $\Delta'$.

(iv) Set $\Delta_2 = \Delta' + \frac{(\Delta_2 - \Delta_1)}{n}, \quad \Delta_1 = \Delta'$

(v) Repeat steps (i) to (iv) above until $|(V - V_c)| \leq \tilde{\epsilon}$ for some small $\tilde{\epsilon}$, subject to $V(V - V_c) \leq 0$ and $|B| \leq |\Delta/3|$.

### C. Solution Refinement

By shooting from a centre to a saddle, we are actually approaching the saddle point from this interior point of the orbit. What results is a solution that has a hydraulic profile with downstream solitary waves appended. As we get closer to the saddle point, these waves will advance further downstream (towards $-\infty$), but in most cases, will still feature in the computed solution. As the computed $\Delta$ is already very precise and the trough of the downstream wave is equal to $-\Delta/3$, we can artificially remove these downstream waves by applying an exponential decay upstream of the first trough encountered in the downstream region. An example of this is given in the top panel of Figure 3. Let $\tilde{B}_s$ be the steady solution of (3) with periodic downstream waves and let $x_k$ be the position of the first downstream trough, i.e. $\tilde{B}'(x_k) = 0$ and $\tilde{B}_s''(x_k) > 0$. Since the asymptotic level of this trough is $-\Delta/3$, upstream of $x_k$ at a point $x_c$ such that $|x_c - x_k| << 1$, we apply the exponential decay:

$$B_1^* = \begin{cases} -\Delta/3 + F_1 e^{(\sqrt{\Delta})x} & x \in [x_u/2, x_c] \\ \tilde{B}_s & x \in [x_c, x_u] \end{cases} \tag{10}$$

where $F_1 = (\tilde{B}_s(x_c) + \Delta/3)e^{-(\sqrt{\Delta})x_c}$.

Now we can use $B_1^*$, valid over $[x_u/2, x_u]$, to construct a periodic solution $B_p$ which shall be defined over $[0, x_u]$. To do this, we first reflect $B_1^*$ so that it spans $[0, x_u/2]$. Then we attach it with the original $B_1^*$ at $x = x_u/2$. An example of this was shown in Figure 1. A linear correction term, $H$, can then be added to $B_p$ to give us the final steady dispersive hydraulic solution, $B_s = B_p + H$. The linearised steady equation (3), can be written, in terms of this corrective function $H$, as

$$H_{xx} + 6B_p H + \Delta H = -R \tag{11}$$

where $R = B_{pxx} + 3{B_p}^2 + \Delta B_p + \gamma f$ is the residue of the solution due to numerical approximation.

As (11) is a linear in $H$, we can use standard matrix methods to obtain a solution. The final periodic solution is obtained on the uniform grid

$$x_j = \frac{x_u(j-1)}{n_u}, \quad j = 1 \ldots n_u \tag{12}$$

and defined on $[0, x_u]$. Then, from Fornberg[14], the Fourier differentiation matrix on this grid is given by

$$D_{ij} = \begin{cases} \dfrac{\pi(-1)^{i-j}}{x_u \tan(\pi(i-j)/n_u)} & i \neq j \\ 0 & i = j. \end{cases} \tag{13}$$

Now, (11) can be written as

$$(D^2 + E)H = R, \tag{14}$$

where $E$ is a diagonal matrix with $E_{j,j} = \Delta + 6B_p(x_j)$. The solution of this can be obtained using standard numerical methods. As illustrated in the bottom panel of Figure 3, the value of the refinement, $H$, at $x = x_u/2$ is effectively zero. This implies that any interaction at the point where the original and reflected solutions meet is negligible.

### D. Branch Following Algorithm

To obtain initial values of $\Delta_2$ and $\Delta_1$ for the minimization routine, a simple branch following algorithm is used. Commencing from a known solution, e.g. $\Delta = 0$ and $\gamma_0 = 0$ or $-8$, an initial estimate is $\Delta_2 = \kappa|\gamma_1 - \gamma_0|^{2/3}$ using appropriate values of $\kappa$ and $\Delta_1 = 0$. Linear and then quadratic interpolation are then used beyond the first point.

## IV. PARAMETRIC RELATIONSHIP FOR DISPERSIVE HYDRAULIC SOLUTIONS

For forcing $f(x) = \text{sech}^2(x)$, the numerical methods outlined in the previous section can now be used to obtain the functional relationship between $\Delta$ and $\gamma$ for the hydraulic type solutions of the fKdV equation. These results are shown in Figures 4 and 5. Provided $n_u$, the number of collocation points, is sufficiently large and $\Delta x$, the grid-spacing, is sufficiently small, the results are largely independent of these latter parameters. For $\gamma < -24.55$, selected values of $\gamma$ show a similar arch-type $\Delta(\gamma)$ relationship as found in $\gamma \in [-24.55, -8]$ and $[-8, 0]$. Therefore, further solutions of compact support may be possible; however as mentioned in Sec. II, no evidence of such solutions has been obtained.

As illustrated in Figure 4, the narrow forcing limit, (5) is in agreement with the computed values as $\gamma \to 0^+, 0^-$ when $K = 2$. For the wide forcing limit, we see that as $\gamma$ increases the relative error, which we shall denote as $|E|$, between the computed $\Delta$ and the analytical formulation $\sqrt{12\gamma}$, valid in the limit $\gamma \to \infty$, tends to zero. The minima in the $\Delta(\gamma)$ curve at $\gamma = -8$ and $\gamma \approx -24.55$ correspond to the forced solitary wave solutions mentioned in Sec. III, the former being the $\text{sech}^2(x)$ solution and the latter a numerically determined solution shown in Figure 5(a).

We conclude this section by considering the form of the solutions as $\gamma$ varies. The key difference is that for $\gamma > 0$ there are no local extrema, whereas all solutions for $\gamma < 0$ have a local maxima. For $\gamma > 0$ as $\gamma$ is increased, the domain in which $B_x$ is non-zero becomes more confined to the region of the topographic perturbation. Consequently since the magnitude of the jump is also increasing along this curve, the magnitude of the slope must also be monotonically increasing. In this limit as $\gamma \to \infty$, it is clear that the response of the fluid, as measured by $B$, becomes a function primarily of the topographic perturbation,

in line with the definition of hydraulic solutions introduced here. Thus we can conclude that dispersion is only a weak effect as $\gamma \to \infty$.

For $\gamma < 0$, it is again apparent that the solutions become confined to the region of the topographic perturbation as $|\gamma| \to \infty$; however, at no stage does dispersion become insignificant and the solutions always remain dispersive hydraulic jumps. If we consider the position of the extrema for these solutions, then it can be shown that in the limit $\gamma \to 0^-$, the extrema must occur far downstream and this approaches the topographic peak from this downstream position as $|\gamma|$ increases. This appears to be a monotonic increase until $\gamma = -8$ at which point the soluion peak coincides with the topographic peak. In the range $-24.55 < \gamma < -8$, the position of the extrema moves downstream and returns to the topographic peak at $\gamma = -24.55$. For $\gamma < -8$, the form of the solution appears to consist primarily of forced symmetric solitary wave in the vicinity of the topographic perturbation coupled to a weak downstream shelf.

## V. LINEAR STABILITY ANALYSIS

### A. Stability Formulation

To determine the stability of the steady solutions, we seek a perturbation variable $C(x, \tau)$ such that $B(x, \tau) = B_s(x) + C(x, \tau)$ satisfies the original evolution equation (1) where $B_s$ is the periodic steady solution discussed in Sec. III. So the full stability equation is

$$C_\tau + ((\Delta + 6B_s)C)_x + 6CC_x + C_{xxx} = 0. \tag{15}$$

Clarke and Grimshaw[15] considered the transcritical propagation of weakly nonlinear and long internal waves through a weak contraction. It was shown that the governing evolution equation for this scenario is the variable coefficient KdV:

$$A_\tau + (\Delta_c A)_x + rAA_x + sA_{xxx} = 0, \tag{16}$$

where $\Delta_c$ describes the velocity perturbation in the contraction. At once, we see that (15) and (16) are identical. Thus, the dispersive hydraulic solutions effectively act as a contraction or expansion in channel width, leading to variable velocity upon which perturbations

propagate. The corresponding nonlinear stability equation for the solitary wave, as discussed by Camassa and Wu[11], also resembles (15). In general, equations of the form (15) or (16) will always be the stability equation for KdV-type problems. The key difference is in the nature of the effective velocity, as represented by $\Delta + 6B_s$ in (15). For solitary wave instability studies, this has a single lengthscale and is confined to a compact region whereas here this term has multiple lengthscales, i.e. the sudden change and plateau between two topographic perturbations.

As we are interested in the linear stability of the steady dispersive hydraulic solutions in this paper, we simply omit the nonlinear term, $6CC_x$ and end up with

$$C_\tau + ((\Delta + 6B_s)C)_x + C_{xxx} = 0. \tag{17}$$

In this section, we shall outline matrix stability methods and direct numerical simulations of the solutions of (16). Consider first the evolution of the perturbation momentum for both (15) and (17). On a periodic domain, this satisfies

$$\frac{dI_1}{dt} + \int_0^{x_u} \frac{\Delta_{cx} C^2}{2} dx = 0, \tag{18}$$

where $I_1 = \int_0^{x_u} \frac{C^2}{2} dx$. Outside of the regions where the topographic perturbation occurs we have $\Delta_{cx} = 0$. Thus, the source of momentum for instabilities is confined to that region where the dispersive hydraulic solitions have near-zero slope. As discussed in the previous section, apart from the limit $\gamma \to 0$, this corresponds to the region of the topographic perturbation.

The conservation law (18) also applies on an infinite domain. In particular, we can draw some conclusions regarding the single topographic perturbation problem on an infinite domain. Most significantly if $\Delta_{cx} \geq 0$ everywhere, then $dI_1/dt \leq 0$ and the steady solution of interest must be stable. Consider the upward jumps for $\gamma > 0$. As pointed out in the previous section, these are monotonic in $x$ and are therefore stable. For other solutions, the minimum of $\Delta_{cx}$ then gives an upper bound on the growth of the perturbation momentum. If we denote

$$\min_x(\Delta_{cx}) = -\Delta_{cx}^*,$$

then we have

$$\frac{dI_1}{dt} = -\int_0^{x_u} \frac{\Delta_{cx} C^2}{2} dx \leq \Delta_{cx}^* I_1$$

and thus $I_1 \leq I_1(0) e^{\Delta_{cx}^* t}$.

Hence a downward jump, i.e. where $A_0 = 0$ downstream, also has a larger bound on the instability growth rate than the corresponding upward jump. Consequently, we would expect, for the periodic solutions considered here, an asymmetry between the growth of instabilities in the original and reflected regions. This law also suggests that the source of instabilities is those regions where $\Delta_{cx} < 0$. For example, consider the solutions in Figure 4 for $\gamma < 0$. Since the extrema for the steady solution always occurs at or downstream of the topographic maxima, this suggests that the primary source of the instability lies between the solution extrema and the topographic extrema.

### B. Matrix Stability Method

As (17) is linear, a solution can be constructed in terms of eigenfunctions. Let

$$C = e^{\lambda t} w(x)$$

then $\lambda$ and $w$ are respectively the eigenvalues and eigenfunctions of

$$\lambda w = -(\Delta w + 6 B_s w + w_{xx})_x. \tag{19}$$

Assuming orthogonality, the complete solution is the sum

$$C = \sum_{j=1}^{\infty} e^{\lambda_j t} w_j(x)$$

On the discrete periodic grid defined by (12), the differential operators are replaced by the Fourier differentiation matrix, $D$, and (19) can be writen as the matrix eigenvalue problem

$$\tilde{M} \times F = \Lambda \times F, \tag{20}$$

where $\Lambda$ is a matrix whose diagonal elements correspond to the eigenvalues of the matrix $\tilde{M} = D \times M$ and is zero everywhere else. The matrix $M = E + D^2$, where $E$ is a diagonal matrix with elements $E_{j,j} = \Delta + 6 B_s(x_j)$ and the Fourier differentiation matrix, $D$, is defined

earlier in Sec. III. The columns of matrix $F$ contain the eigenvectors of $\tilde{M}$. Standard matrix methods can then be used to solve (20).

Typically, the eigenvalue spectrum is similar to that found in Pego and Weinstein[10], which consist of a discrete spectrum of modes whose real part are effectively zero and finite number of growing modes, for each of which a corresponding decaying mode also occurs. The eigenvalues also have complex conjugate symmetry, and thus, away from the continuous spectrum, occur as real pairs or complex quartets. In order to characterize the linear stability, we seek the fastest growing eigenmode, $\sigma$, such that

$$\sigma_r = \sup_{j \in n_u} Re(\lambda_j).$$

From the matrix stability method, we can therefore characterize the steady dispersive hydraulic solutions of Sec. IV as stable if $\sigma_r$ is effectively zero (e.g. $10^{-8}$ or smaller) and unstable otherwise. The spectrum of $\sigma_r$ values are given in Figure 6 when three different grid sizes of $\Delta x$ were considered.

Consider the effect of a change in domain size on the spectrum, which could be due to either a change in $\Delta x$ or $n_u$. The primary result of this is a phase shift of the $\sigma_r$ spectrum. For example, the spectrum for $\gamma = -17.5$ is illustrated in Figure 6(b). Here, $\sigma_r$ is a local minimum when $x_u = 170.7$ and a local maximum when $x_u = 256$. In Figure 7, the effect of varying the grid size (and hence domain variation) on the computation of $\sigma_r$ is shown for two values of $\gamma$.

For fixed $\gamma$, we can define the envelope of this phase shift as the local extrema of $\sigma_r$ as the size of the domain is varied over a small range. Therefore, if $\gamma$ and $x_u$ are fixed, the upper and lower limits of the envelope can be respectively defined as:

$$Re(\overline{\sigma}_{max}(\gamma)) = \sup_{L \in [L-\delta, L+\delta]} \sigma_r(\gamma, L),$$

$$Re(\overline{\sigma}_{min}(\gamma)) = \inf_{L \in [L-\delta, L+\delta]} \sigma_r(\gamma, L).$$

where $\delta << x_u$. This envelope is apparent in Figure 6 and we would expect that as more domain sizes are used in the given ranges, the envelope would become more pronounced. At $\gamma = -8$ and $-24.55$, the envelope decreases to zero width indicating that the instability results for those values are largely independent of domain size. Also it is clear that for

$n_u = 1024$, the width of the envelope is smaller than the corresponding results for $n_u = 512$ indicating that the dependence on the domain size decreases as the domain size increases. Consequently, we will confine our comments on instability to these larger domain sizes from here.

The phase shift in the oscillations can be investigated for fixed $\gamma$ as a function of domain size. One example each for positive and negative $\gamma$ is given in Figure 7. In doing so, it is useful to also consider the behaviour of the next largest eigenvalue (based on the real part). Figure 7(a) demonstrates the general evolution of the eigenvalues as a function of domain size. This behaviour appears to be that a quartet of eigenvalues are generated from the continuous spectrum. The imaginary part increases while the real part reaches a maximum and then decreases and the quartet is reabsorbed into the continuous spectrum at a larger value of domain size. Consequently, the spectrum observed for $\sigma_r$ is a superposition of contributions from many different eigenvalues. This is most significant at points where the dominant and sub-dominant eigenvalues have approximately equal real parts. For example, this occurs at $\Delta x = 0.24, 0.253$ and 0.26 in Figure 7(a) and at $\Delta x = 0.147$ and 0.2 in Figure 7(b). We will return to this point later.

As evident by the positive leading eigenvalues, given by $\sigma_r$, the matrix stability analysis shows that we have linear instability for all $\gamma$ values. The instability can be described as weak, as $\sigma_r$ is relatively small and always smaller than the value for $\gamma = -8$. For the solitary wave solution at $\gamma = -8$, our linear instability characterization is in agreement with the solitary wave instability results by Camassa and Wu[11]. In addition, it should be noted that when $\Delta = 0$, i.e. at $\gamma = -8$ and approximately $-24.55$, the eigenvalues $\sigma_r, Re(\overline{\sigma}_{max}), Re(\overline{\sigma}_{min})$ are all equal and strictly real.

Although it is not possible to associate eigenvalues with the downward jump in the reflected region and the upward jump in the original region, we can expect from our earlier comments of the evolution of $I_1$, for there to be asymmetry related to the linear instability. In particular for $\gamma > 0$ since the upward jumps are monotonically increasing, this suggests that the instability is purely associated with the downward jump. For $\gamma < 0$, the upward jumps are no longer monotonically increasing and so instability cannot be ruled out. However, we would expect growth associated with an upward jump to be slower than that for the corresponding downward jump.

To see the implication of this eigenvalue variation (or lack thereof) on the eigenfunctions,

we turn to Figure 8. In plots (a) to (h) of this figure, we see that waves are formed in the regions $x > 0.75x_u$ and $x < 0.25x_u$, which will have a wavenumber $k = \sqrt{\Delta}$. The modulation of these waves is a result of changing $\Delta x$ and consequently $x_u$ which in turn, changes the dominant eigenfunction. At discrete values of $x_u$, the upstream and downstream phase match and consequently, optimal growth occurs. Between these discrete values, the phase of the dominant eigenfunctions do not match and sub-optimal growth occurs.

Consequently, the eigenfunctions profiled in Figure 8(c-h) have modulated periodic motion in the region $x > 0.75x_u$ and $x < 0.25x_u$. In contrast for points around $\Delta = 0$, waves in the regions $x > 0.75x_u$ and $x < 0.25x_u$ are not as significant as $k,\ \Delta \to 0$. Hence around $\gamma = -8$, where $\Delta$ is effectively zero, there is no variation in the eigenvalue envelope. This also holds for $\gamma \approx -24.55$ where $\Delta \approx 0$.

Consider now the variation of eigenvalues with domain size and the effect on direct numerical simulations. These are accomplished here using standard numerical techniques, see Clarke and Grimshaw[3]. Spatial differentiation is accomplished using fast fourier transforms[14], and temporal integration using a fourth order Runge-Kutta method. For a given $B_s(x, \gamma)$ and $\Delta(\gamma)$, the initial condition used for $C$ is a random initial field normalized to lie between $[-0.01, 0.01]$.

The evolution of $I_1$ for fixed $n_u$ and $\gamma$ but varying $\Delta x$ (and consequently $x_u$) is shown in Figures 9 and 10. For a random initial field after sufficiently large time, the average growth for the linear perturbation momentum is $O(e^{2\sigma_r t})$ for all $\gamma$ being considered. This average behaviour is clearly observed for both figures. When we impose the real part of the eigenfunction associated with $\sigma_r$ as the initial condition, we see that these oscillations and variations in $I_1$ no longer occur and the linear perturbation momentum grows according to $O(e^{2\sigma_r t})$ throughout the numerical simulation.

In relating Figures 7, 9(a-b) and 10(a-b), we see that when $\sigma_r$ is a local maximum for a particular value of $\gamma$, there are effectively no oscillations in the perturbation momentum evolution for sufficiently large time, whereas we observe oscillations of varying frequency for other $\sigma_r$ values. To better understand this, we turn to the evolution of perturbation variable, $C$.

At the local maxima of $\sigma_r$, the evolution plots demonstrate that the behaviour is either steady growth (ref. Figure 9(c)) or steady propagation of wavepackets through the domain (ref. Figure 10(c)). Near the local minima of $\sigma_r$, the propagation of wavepackets through

the domain still occur; however, a temporal modulation occurring with the oscillatory period observed in the evolution of $I_1$ is superimposed. This can be observed in Figures 10(d) and 9(d). From Figure 7, it is clear that the reason for this is due to the fact that at local maxima of the $\sigma_r$ spectrum, we have the dominant growth of a unique mode whereas at a local minima in the spectrum, the coupled growth of two modes with differing imaginary parts occurs. An estimate of the period of these oscillations in $I_1$ and $C$ can be obtained from the spectrum of $\sigma_r$ shown in Figure 7. If two eigenvalues have similar real part, then we would expect that the period of oscillations due to interactions between the two modes will be:

$$T = \frac{2\pi}{\lambda_{id}}, \tag{21}$$

where $\lambda_{id} = Im(\lambda_1) - Im(\lambda_2)$. From Figure 9(b) and Figure 7(b), $\lambda_d = 0.0781$ and $T = 80$ based on approximately 2.5 cycles within $t \in [400, 600]$. This latter value is 0.56 percent off the theoretical value. For Figure 10(b) and from Figure 7(d), $\lambda_{id} = 0.196$ and $T = 33.33$ based on approximately 6 cycles within $t \in [600, 800]$. This latter value is 3.97 percent off the theoretical value.

## VI. CONCLUSION

The main result of this paper has been to investigate a family of solutions of the fKdV equation which are flat both upstream and downstream of a confined topographic perturbation, but which in general have differing limits. We refer to these jump solutions as dispersive hydraulic flows. The impetus for this has been to provide a continuous spectrum of solutions to supplement the limits used by GS to construct approximate solutions to the initial value problem for the fKdV equation. By a transformation of the detuning parameter, $\Delta$, a one-parameter family of solutions has been obtained, whereas the solutions of GS occupy a phase-plane. Therefore, we must first determine the relationship between our solutions and those of GS. The fKdV equation has the energy conservation property

$$\frac{d}{d\tau}\int_{-\infty}^{\infty} B dx = 0.$$

This suggests that the solutions should be able to form, provided $B$ is of opposite sign far upstream and downstream of a jump. If $B$ has the same value upstream and downstream,

then energy cannot be conserved for finite energy initial conditions. Let $\Delta^*(\gamma)$ be the locus of our one-parameter family of solutions when $B = 0$ upstream of an upward jump. The downstream level is then $B_d = -\Delta^*/3$. Thus, conservation of energy states that the allowable limits of the upstream level are $[-\Delta^*/3, 0]$, while the corresponding limits of the downstream level are $[0, \Delta^*/3]$. For downward jumps, these limits are reversed. Hence, the dispersive hydraulic solutions are a feasible asymptotic solution of the fKdV equation for $-\Delta^* \leq \Delta \leq \Delta^*$. In Figure 11, this range of solutions is shown in comparison with the boundaries of GS regimes for the same topography.

For $\gamma > 0$, it is apparent that the solutions obtained here are in good agreement with the GS boundaries, except where $|\Delta|$ becomes large. In both these limits, this appears to be due to the fact that alternative steady solutions exist which are preferential attractors for the initial value problem. For negative $\Delta$, GS demonstrated that in the transition regime, the solution consisted of a steady wavetrain downstream of the topography and an upstream plateau. When $\Delta$ is positive, supercritical solutions which are largely symmetric about the topographic maximum were obtained. Interestingly, no such supercritical or subcritical solutions were obtained for positive $\gamma$, even though they are allowable with this method. The only such solutions are for $\gamma = -8, -24.55$. Since the stability of these dispersive hydraulic solutions have been established, this indicates that the final state is clearly dependent on the initial condition.

For negative $\gamma$, no agreement between the solutions outlined here and the regimes of GS occurs. In this region, the relevant solutions compatible with the short time asymptotics for the trivial initial condition are the downward jump solutions, which appear to be the most linearly unstable of the four types of jump solutions considered. Coincidentally in this regime, the solutions of GS, both in the resonant and transition regimes are unsteady. It is therefore of interest to understand the long-time nonlinear evolution of solutions in this region. In particular, do unsteady solutions similar to those of GS evolve, or do alternative unsteady states exist.

For both negative and positive $\gamma$, there also exist complementary solutions to those compatible with the fKdV equation trivial initial value problem. For negative $\gamma$, this is the upward jump solution and for positive $\gamma$, the downward jump solution. The latter case is not of particular interest as the downward jump solutions are linearly unstable whereas the upward jump solutions are stable. For the former case, we would expect the upward jump

solutions to have a weaker instability than the downward jump solutions. Consequently, their asymptotic evolution is also of interest.

One other approach that has been used to investigate the linear stability of the solutions investigated here is the momentum integral derivative. As discussed in the introduction, this method has been used by Pego and Weinstein[10] and others to characterize the stability of forced and unforced compact solutions of KdV type equations. Unfortunately, most probably due to the fact that the solutions being investigated here do not have compact support, there is no correlation between the results of this method and the matrix stability results.

As mentioned in Sec. I, Dias and Vanden-Broeck[8] considered periodic hydraulic type solutions. The periodicity of these solutions was made possible by the presence of a second identical topographic perturbation which reversed the first hydraulic transition. The solutions presented here, where the original solution is reflected, are a limiting example of the solutions of Dias and Vanden-Broeck[8] when there are no waves between the two perturbations. Two comments can be made regarding these solutions. The first is that identical topographic perturbations are not necessary to reverse a dispersive hydraulic transition. In fact, to construct asymmetric periodic solutions, one only needs to draw a horizontal line through Figures 4 and 11. The intersection of the $\Delta(\gamma)$ curve then gives dispersive hydraulic solutions with identical downstream levels. Thus, we can construct solutions with non-matching pairs as illustrated in Figure 12. Secondly, at least for the limiting examples considered here, the periodic hydraulic type solutions of Dias and Vanden-Broeck[8] would appear to be linearly unstable. In particular, this instability would be expected to be fastest growing for the downward jump. Again, the nonlinear evolution of such solutions is of interest.

[1] P. G. Baines, "Topographic Effects in Stratified Flows", (Cambridge University Press, 1998).

[2] P. D. Killworth, "On hydraulic control in a stratified fluid", J. Fluid Mech., **237**, 605 (1992)

[3] S. R. Clarke and R. H. J. Grimshaw, "Resonantly generated internal waves in a contraction", J. Fluid Mech., **274**, 139 (1994)

[4] R. H. J. Grimshaw and N. Smyth, "Resonant flow of stratified fluid over topography", J. Fluid Mech., **169**, 429 (1986)

[5] F. Dias and J. M. Vanden-Broeck, "Generalized critical free surface flows", J. Engrg Math., **42**, 291 (2002)

[6] F. Dias and J. M. Vanden-Broeck, "Steady two-layer flows over an obstacle", Phil. Trans. R. Soc. Lond. A, **360**, 2137 (2002)

[7] F. Dias and J. M. Vanden-Broeck, "Two-layer hydraulic falls over an obstacle", Eur. J. Mech. B Fluids, **23**, 879 (2004)

[8] F. Dias and J. M. Vanden-Broeck, "Trapped waves between submerged obstacles", J. Fluid Mech., **509**, 93 (2004)

[9] J. L. Bona, P. E. Souganidis and W. A. Strauss, "Stability and Instability of Solitary Waves of Korteweg-de Vries type",Proc. R. Soc. London Ser. A, **411**, 395 (1987)

[10] R. L. Pego and M. I. Weinstein, "Eigenvalues and Instabilities of Solitary Waves", Phil. Trans. R. Soc. Lond. A, **340**, 47 (1992)

[11] R. Camassa and T. Y. Wu, "Stability of forced steady solitary waves", Phil. Trans. R. Soc. Lond. A, **337**, 429 (1991)

[12] D. E. Pelinovsky and R. H. J. Grimshaw, "Instability Analysis of internal solitary waves in a nearly uniformly stratified fluid", Phys. Fluids, **9**, 3343 (1997)

[13] J. R. Dormund and P. J. Prince, "A family of embedded Runge-Kutta formulae", J. Comp. Appl. Math, **6**, 19 (1980)

[14] B. Fornberg, "A practical guide to pseudospectral methods", (Cambridge University Press, 1995)

[15] S. R. Clarke and R. H. J. Grimshaw, "Weakly nonlinear internal wave fronts", J. Fluid Mech., **415**, 323 (2000)

Figure captions

- Figure 1 - Numerical solution to (3) for both the (i) original solution region defined over $[x_u/2, x_u]$ with $x_p = 128$ and (ii) reflected solution region defined over $[0, x_u/2]$ with $x_p = 42.67$, subject to $\gamma = -4,\ \Delta = 2.584,\ x_u = 512/3$.

- Figure 2 - Top panel: Using $\Delta = 3$ a sketch of homoclinic orbits of the KdV equation with centre at $B = 0$ and saddle point at $B = -1$ corresponding to far-field upstream and downstream amplitudes. Bottom panel: sketch of corresponding potential V where $B_x = 0$ and $f = 0$ showing the centre and saddle points.

- Figure 3 - Top panel: Numerical solution to (3) over original region defined over $[x_u/2, x_u]$, where $\Delta = 2.5854,\ \gamma = -4,\ x_u = 512/3$. Before applying exponential decay (solid line), after the application of exponential decay (dashed) and the point of the application of the exponential decay denoted by asterisk. Bottom panel: Semilog plot of residue solution $H$, in original region defined over $[x_u/2, x_u]$, to (3), $\Delta = 2.5854$, $\gamma = -4,\ x_u = 512/3$ and $x_p = 128$. The point of application of the exponential decay on the numerical solution is denoted by the asterisk.

- Figure 4 - Plot of $\gamma$ vs $\Delta$ using $n_u = 512$ and $\Delta x = 1/4$. This describes the locus of dispersive hydraulic solutions for (3). Corresponding absolute value of relative error $|E|$ (bottom panels) between our computed $\Delta$ and that in GS, to verify the (a) narrow forcing limit and (b) wide forcing limit, both using $n_u = 512$ and $\Delta x = 1/4$.

- Figure 5 - Numerical solution of (3) after solution refinement with $x_p = 32$ and using (a): $\gamma = -24.55$, (b): $\gamma = -20.45$, (c): $\gamma = -17.65$, (d): $\gamma = -12.15$, (e): $\gamma = -5.95$, (f): $\gamma = -3.05$, (g): $\gamma = -1.95$, (h): $\gamma = 1.25$, (i): $\gamma = 3.75$. Solutions (a) to (i) have each been displaced such that the upstream level corresponds to zero.

- Figure 6 - Plots of eigenvalue spectra, $\sigma_r$ vs $\gamma$ formed by combining the eigenvalue plots using (a) $n_u = 512$, $x_u = 128,\ 102.4,\ 85.3$ and (b) $n_u = 1024$, $x_u = 256,\ 204.8,\ 170.6$. $\sigma$ is the eigenvalue with the largest real part which can be obtained after solving (20). Smaller box embedded in the bottom panel is a zoomed plot of the spectra for $\gamma \in [-18, -17]$.

- Figure 7 - Plots of the $Re(\lambda)$ and $Im(\lambda)$ vs $\Delta x$ using $n_u = 1024$ of the two leading eigenvalues, obtained after solving (20), ranked according to the size of the real components. (a-b): $\gamma = 3.5$ and (c-d): $\gamma = -5$.

- Figure 8 - Plots of $Re(w)$ and $Im(w)$: real and imaginary components of the eigenfunction associated with $\sigma$, the eigenvalue with the largest real part which can be obtained after solving (20). (a-b): $\gamma = -5, \quad x_u = 170.66$, (c-d): $\gamma = -5, \quad x_u = 256$, (e-f): $\gamma = 3.5, \quad x_u = 246.7$, (g-h): $\gamma = 3.5, \quad x_u = 265.9$, (i): $\gamma = -8, \ x_u = 256$. The solutions all have mean value zero but have been displaced for clarity.

- Figure 9 - Logarithmic scale plot of perturbation momentum vs time over combined region $[0, x_u]$, using $n_u = 1024$ and $\gamma = -5$ for (a): $\Delta x = 0.167$, $\sigma = 0.02802 + 5.090i$ and (b): $\Delta x = 0.25$, $\sigma = 0.01718 + 0.5467i$. The dotted lines show the exponential growth due to $\sigma_r$. Normalized numerical solutions to (17) with $n_u = 1024$ and $\gamma = -5$ for (c): $\Delta x = 0.167$, $\sigma = 0.02802 + 5.090i$ and (d): $\Delta x = 0.25$, $\sigma = 0.01718 + 0.5467i$.

- Figure 10 - Logarithmic scale plot of perturbation momentum vs time over combined region $[0, x_u]$, using $n_u = 1024$ and $\gamma = 3.5$ for (a): $\Delta x = 0.2409$, $\sigma = 0.01907 + 2.109i$ and (b): $\Delta x = 0.2597$, $\sigma = 0.01563 + 1.570i$. The dotted lines show the exponential growth due to $\sigma_r$. Normalized numerical solutions to (17) with $n_u = 1024$ and $\gamma = 3.5$ for (c): $\Delta x = 0.2409$, $\sigma = 0.01907 + 2.109i$ and (d): $\Delta x = 0.2597$, $\sigma = 0.01563 + 1.570i$.

- Figure 11 - A depiction of the parameter space for solutions of (1) for $f = \text{sech}^2(x)$. The dashed lines and text denote denote asymptotic regimes for the solutions of (1) for the trivial initial condition. The solid lines and shading depict allowable boundaries for the dispersive hydraulic solutions considered here.

- Figure 12 - Numerical solution of (3) after solution refinement with $x_p = -32, 32, 96$, $n_u = 512$ along with topographic perturbations using $\gamma = -10.25$, $\gamma = -7.85$ and $\gamma = 0.05$.

**Figures**

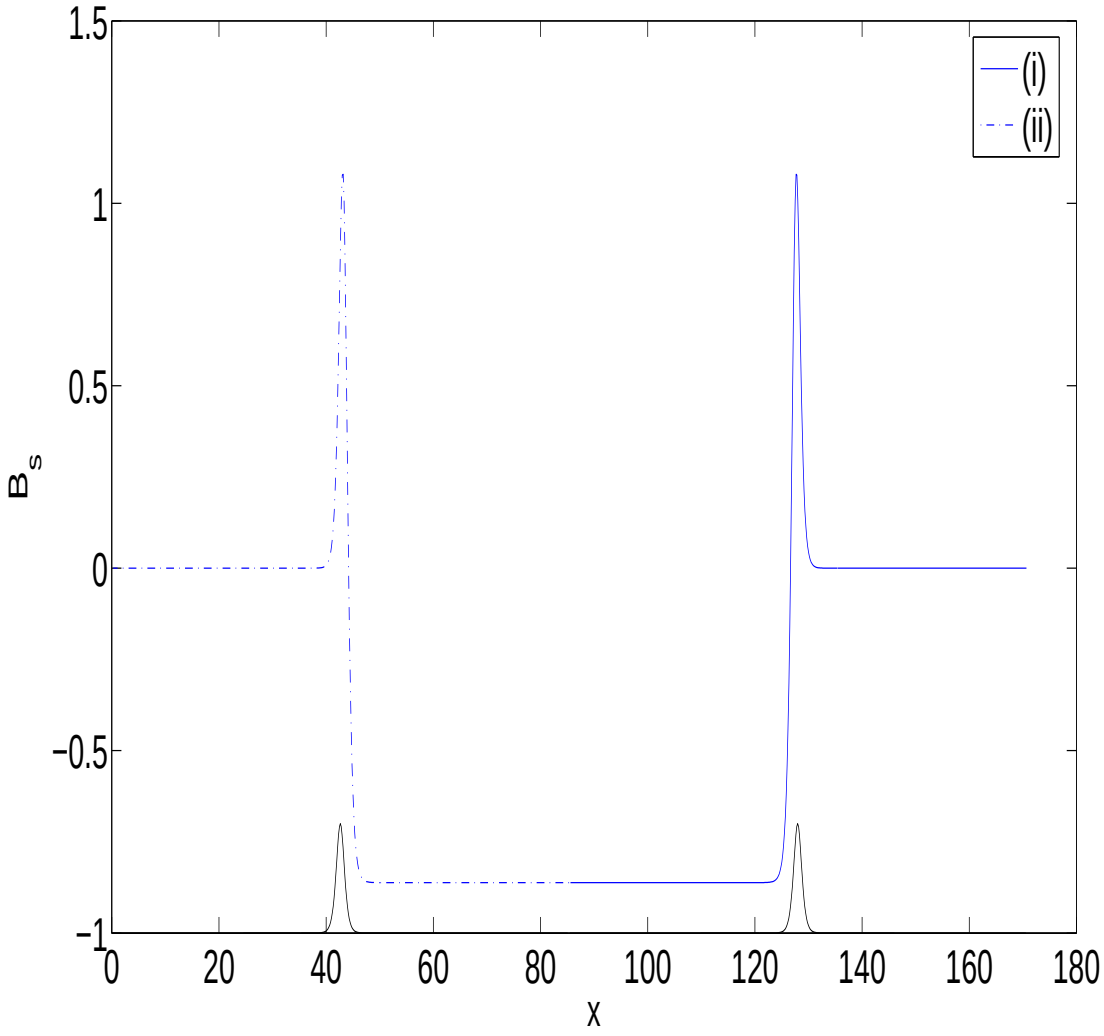


FIG. 1:

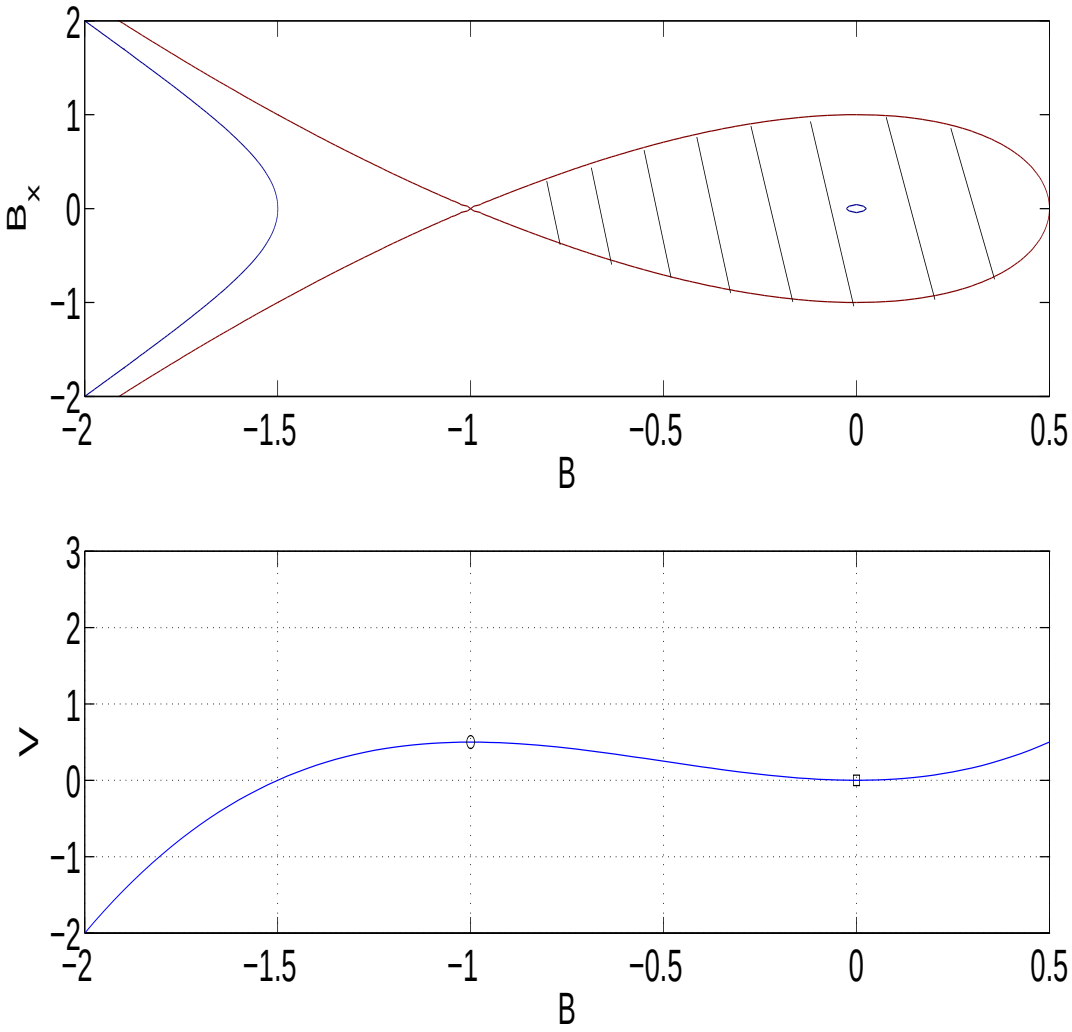


FIG. 2:

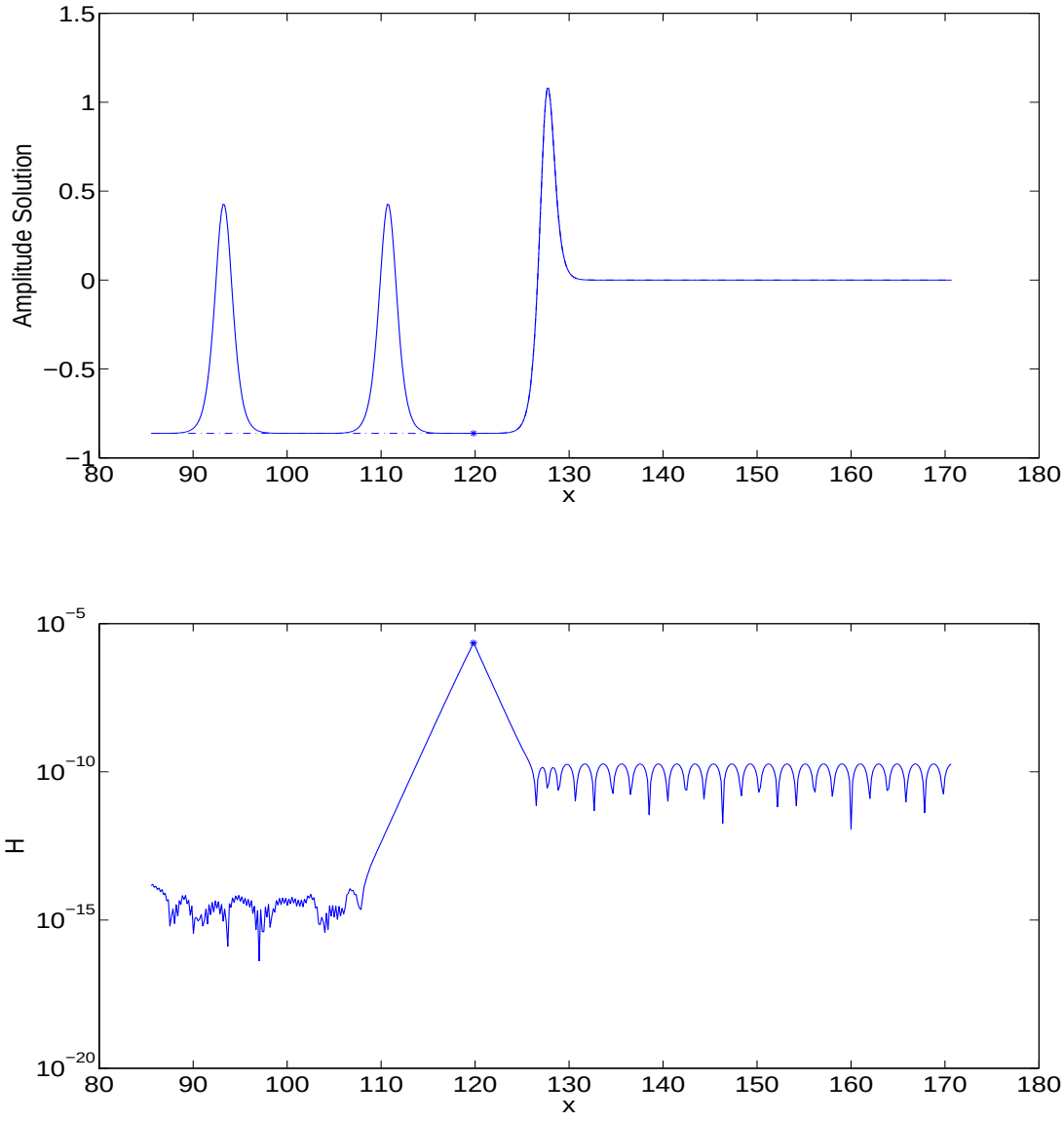


FIG. 3:

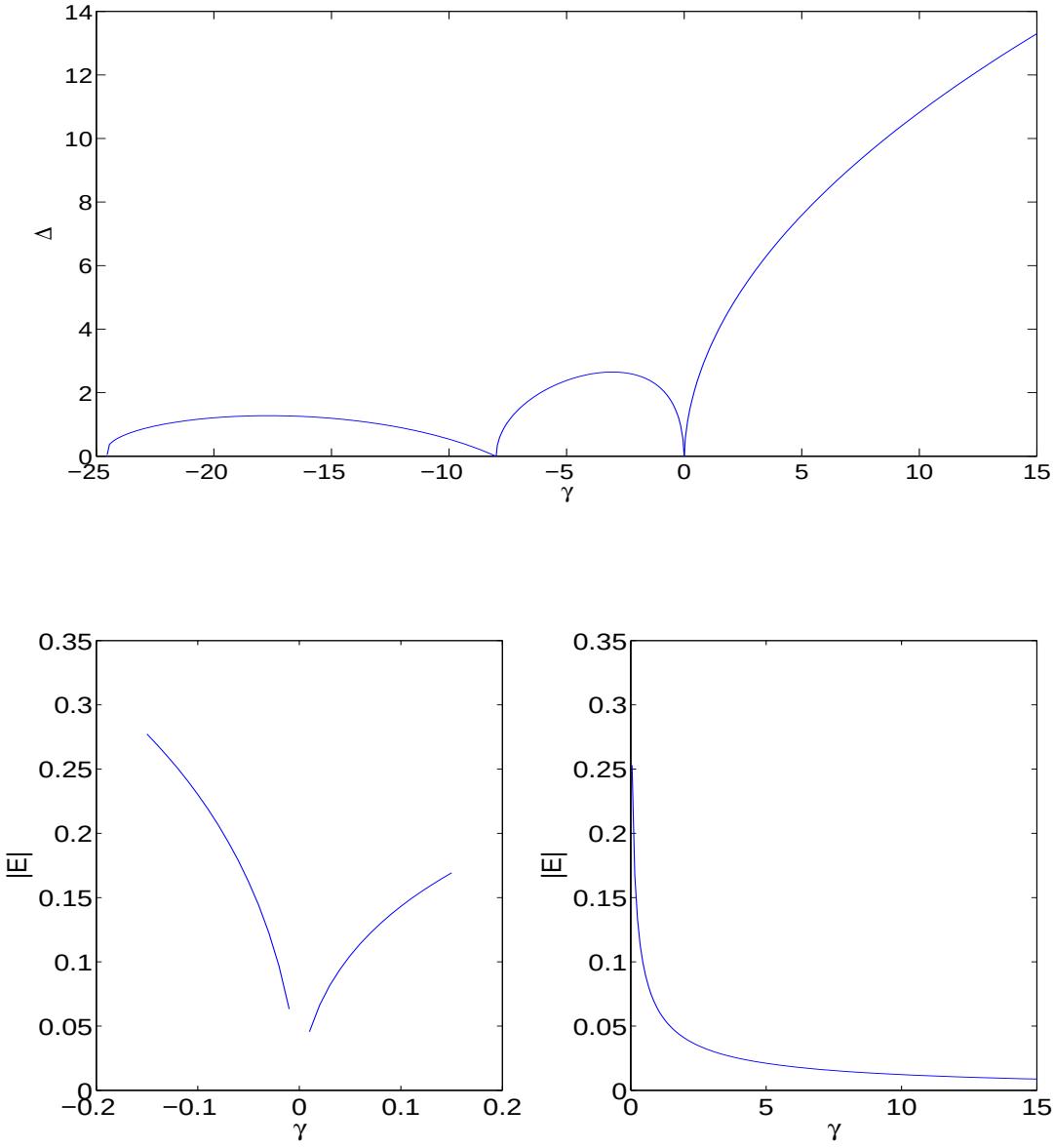


FIG. 4:

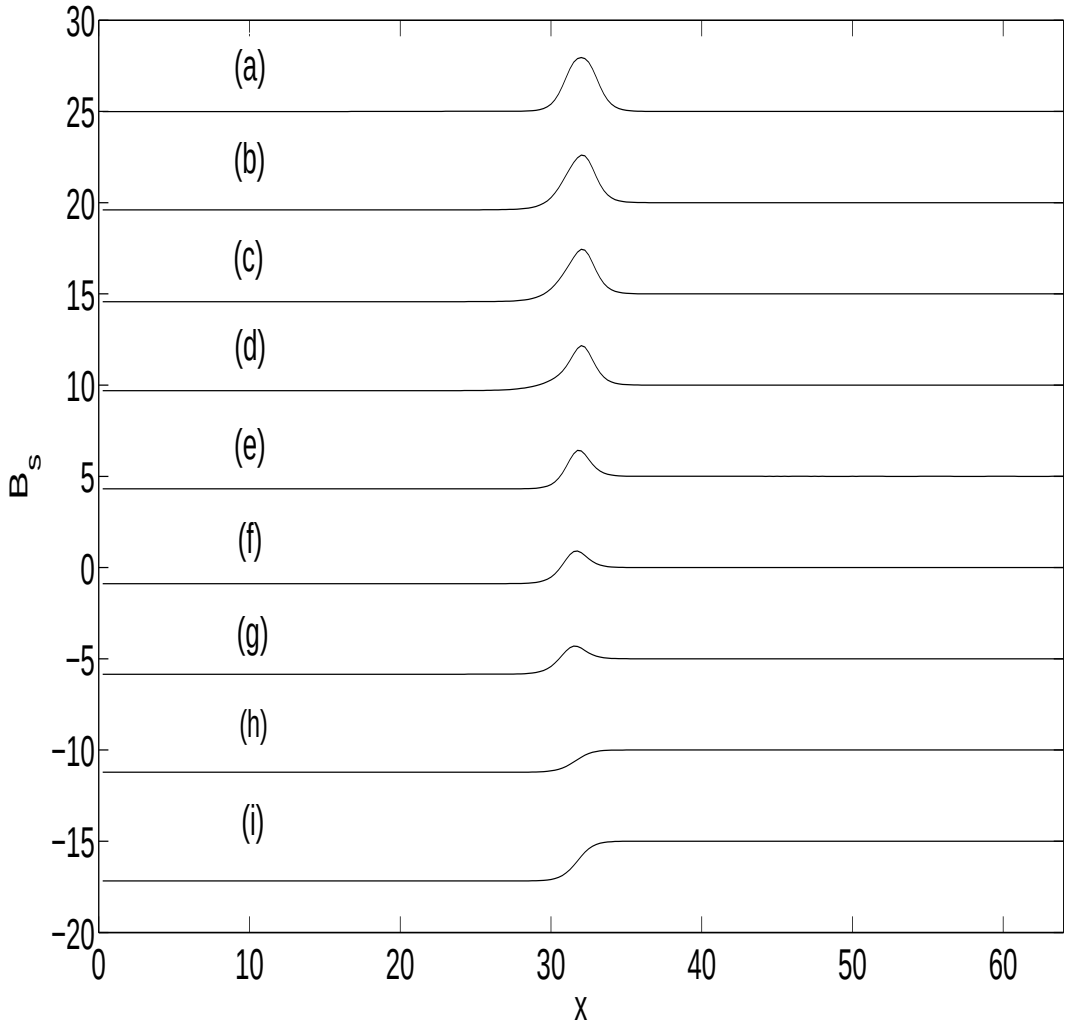


FIG. 5:

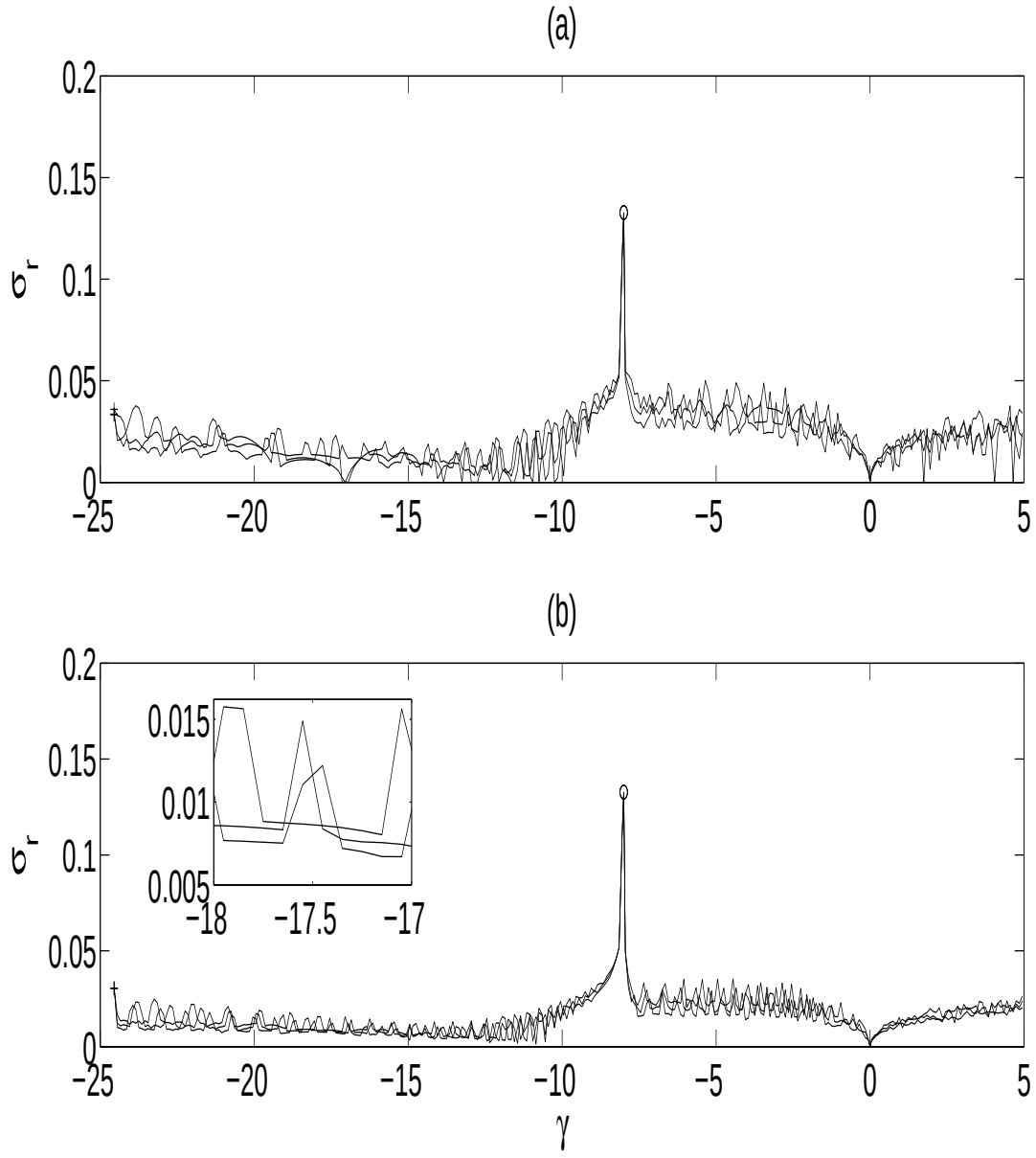
(a)
0.2
0.15
0.1
0.05
0
$\sigma_r$
−25
−20
−15
−10
−5
0
5
(b)
0.2
0.15
0.1
0.05
0
$\sigma_r$
0.015
0.01
0.005
−18
−17.5
−17
−25
−20
−15
−10
−5
0
5
γ

FIG. 6:

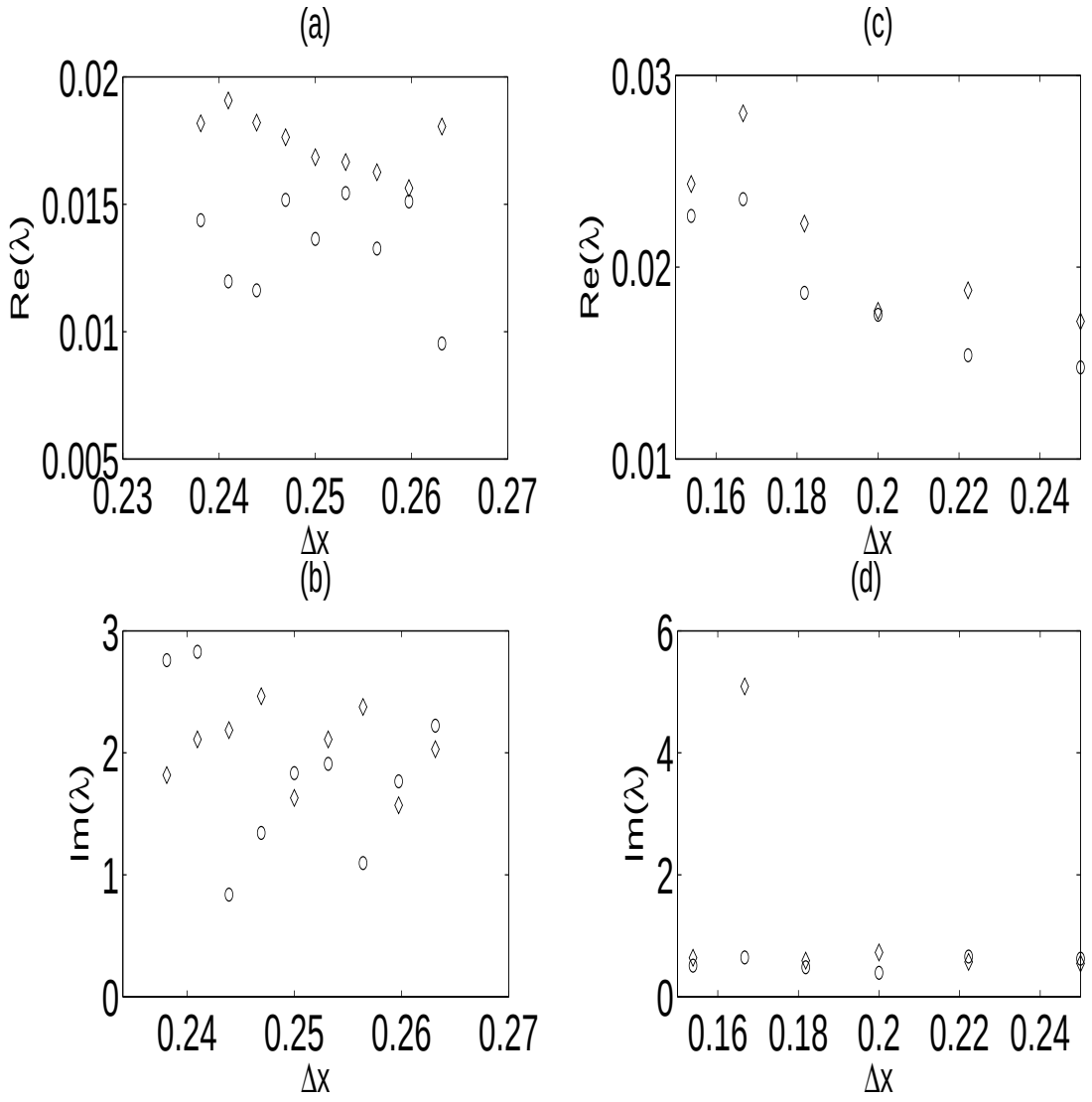
(a)
(c)
(b)
(d)
Re(λ)
Im(λ)
Δx
0.02
0.015
0.01
0.005
0.03
0.02
0.01
3
2
1
0
6
4
2
0
0.23
0.24
0.25
0.26
0.27
0.16
0.18
0.2
0.22
0.24

FIG. 7:

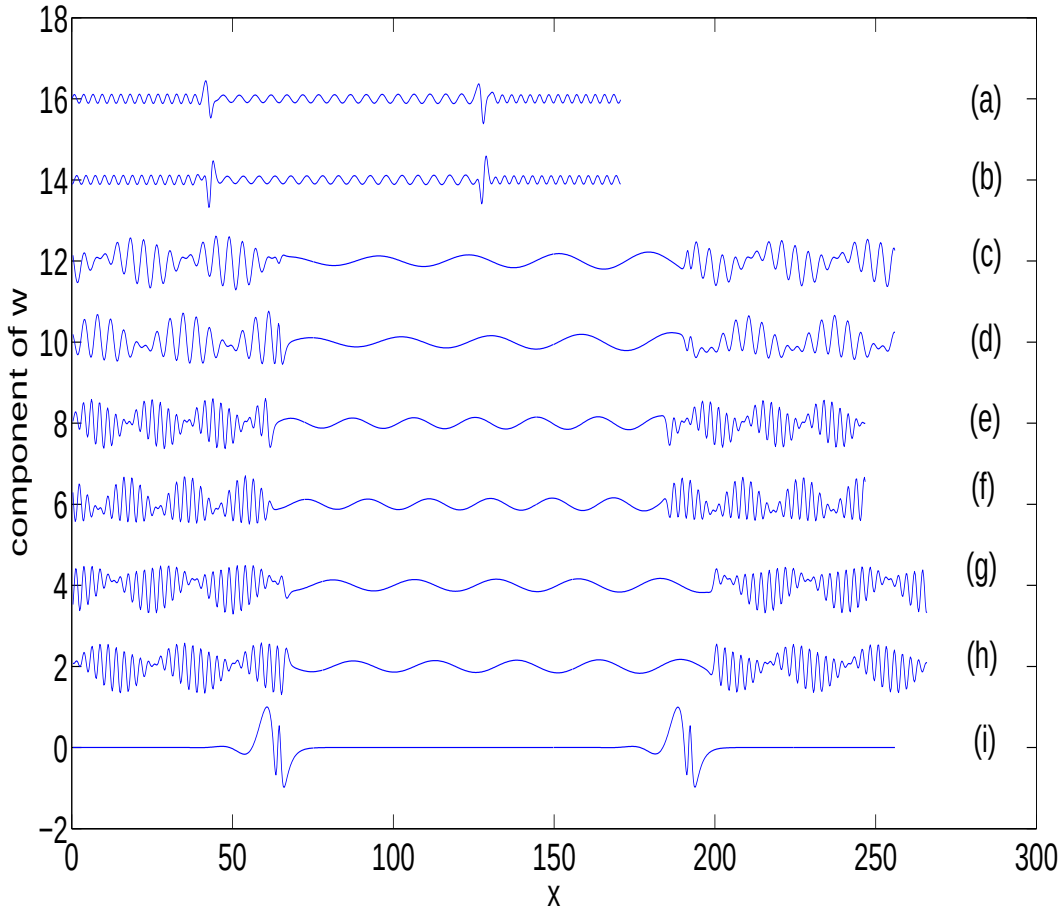
component of w
x
(a)
(b)
(c)
(d)
(e)
(f)
(g)
(h)
(i)
18
16
14
12
10
8
6
4
2
0
−2
0
50
100
150
200
250
300

FIG. 8:

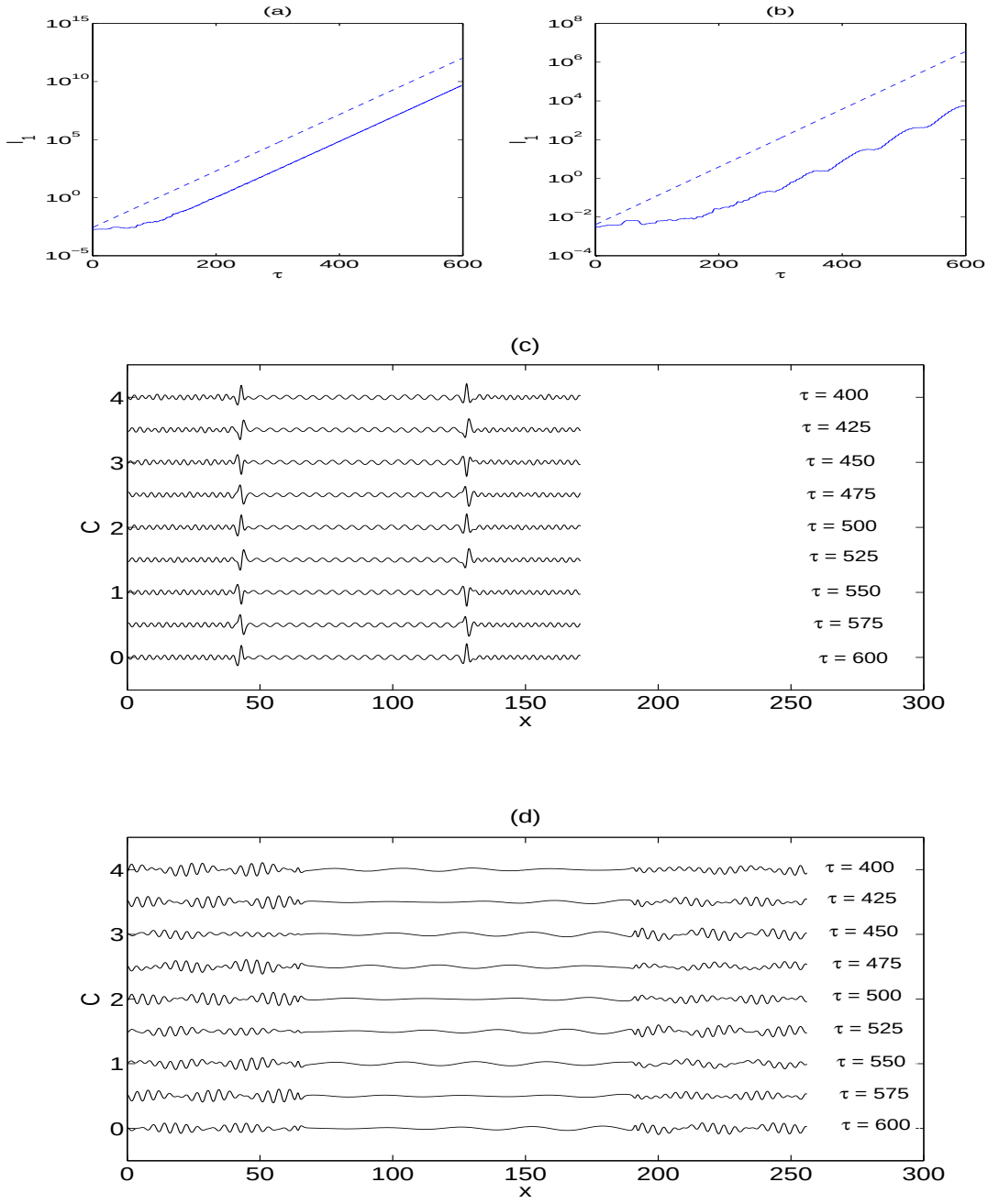
(a)
(b)
(c)
(d)
$l_1$
τ
C
x
τ = 400
τ = 425
τ = 450
τ = 475
τ = 500
τ = 525
τ = 550
τ = 575
τ = 600

FIG. 9:

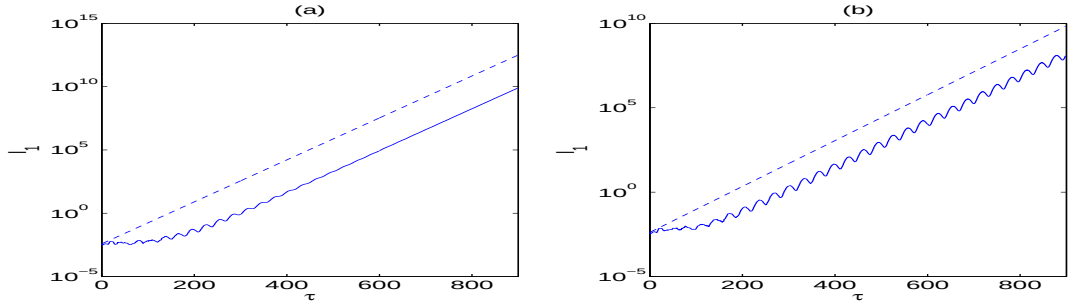
(a)
(b)
$l_1$
τ

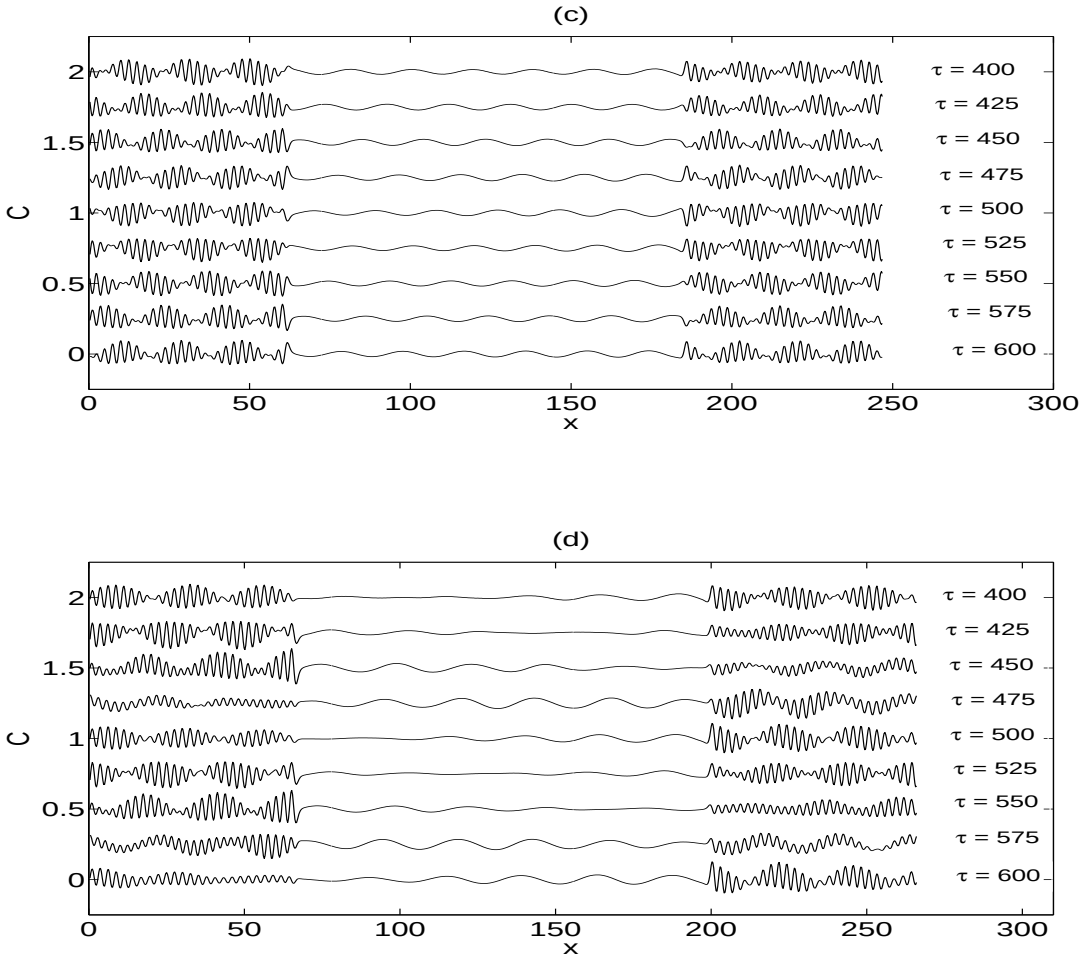
(c)
C
x
τ = 400
τ = 425
τ = 450
τ = 475
τ = 500
τ = 525
τ = 550
τ = 575
τ = 600
0
0.5
1
1.5
2
0
50
100
150
200
250
300


(d)
C
x
τ = 400
τ = 425
τ = 450
τ = 475
τ = 500
τ = 525
τ = 550
τ = 575
τ = 600
0
0.5
1
1.5
2
0
50
100
150
200
250
300

FIG. 10:

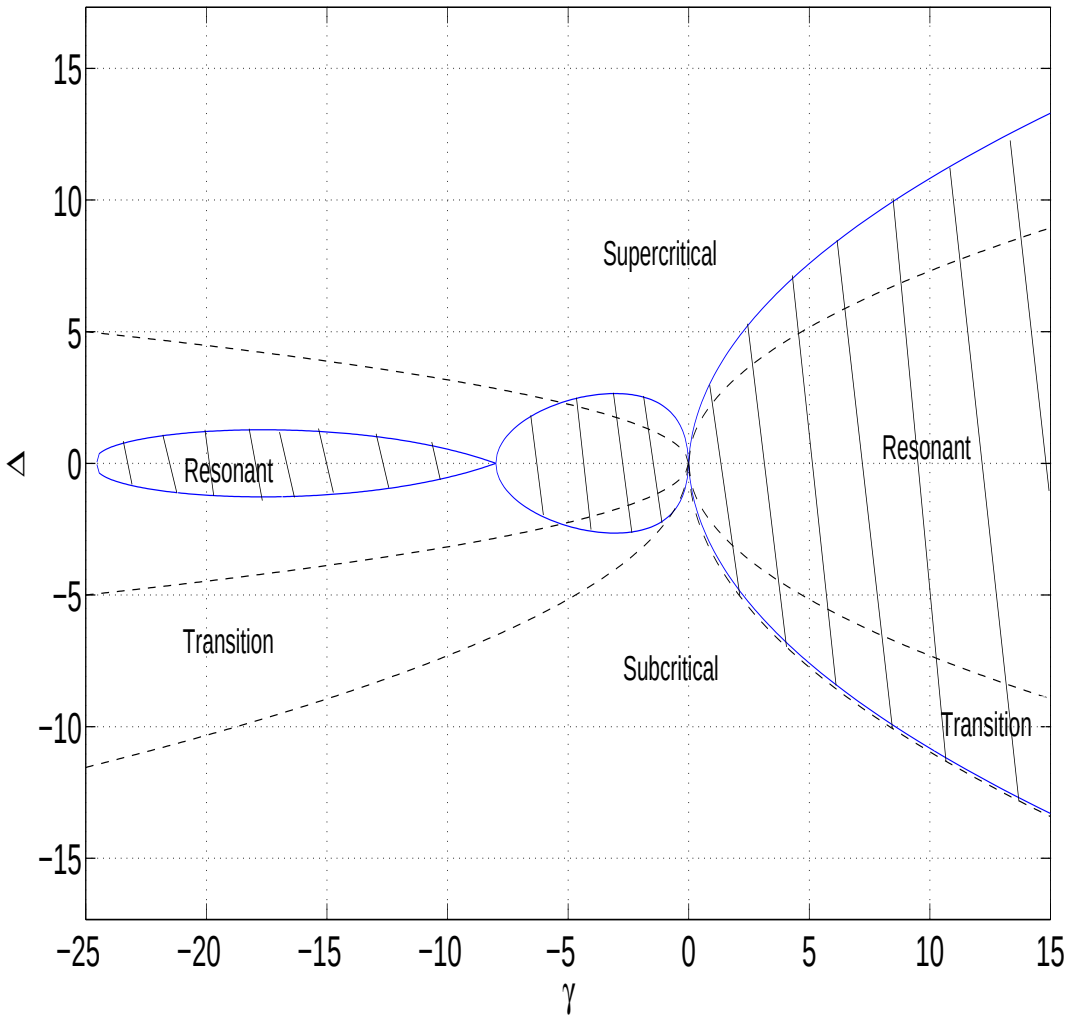
Supercritical
Resonant
Resonant
Transition
Subcritical
Transition
Δ
γ
15
10
5
0
−5
−10
−15
−25
−20
−15
−10
−5
0
5
10
15

FIG. 11:

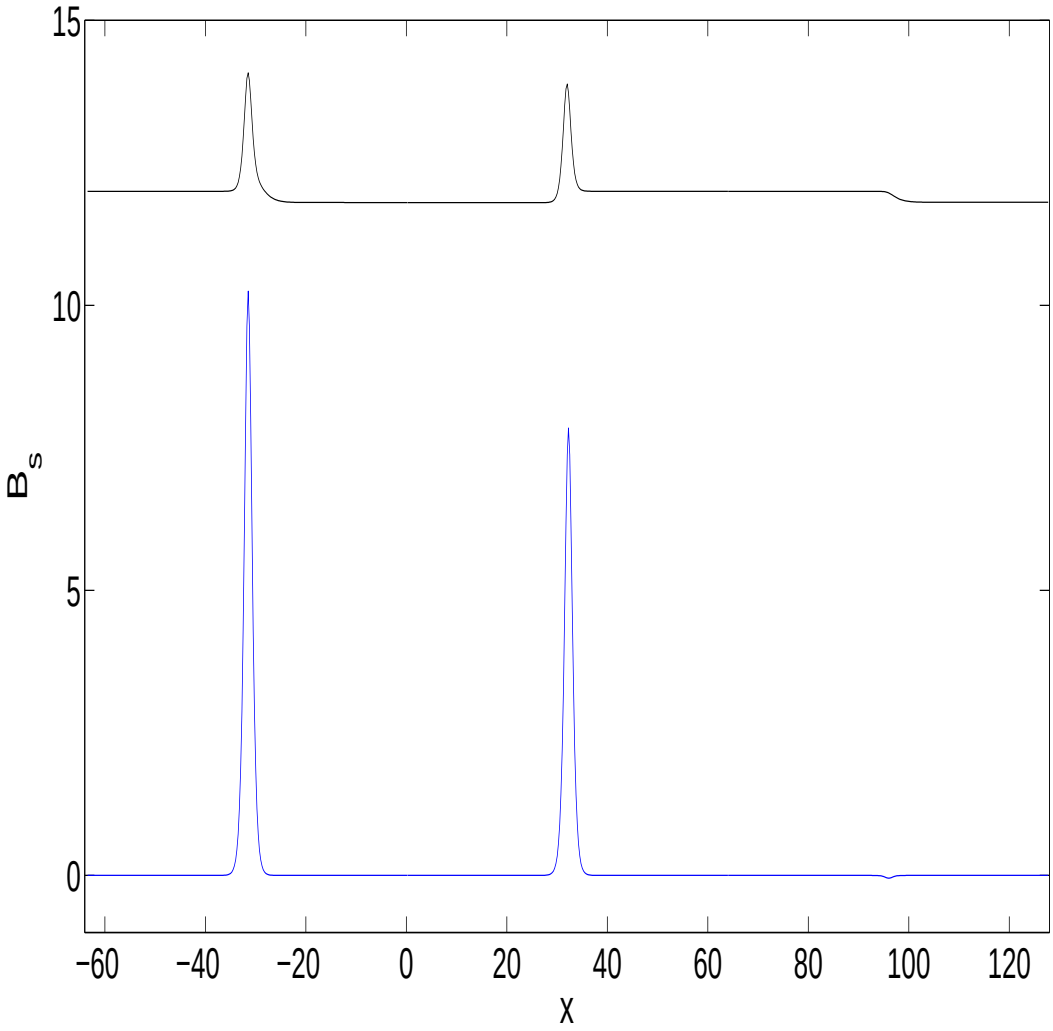


FIG. 12: